POLITECNICO DI TORINO
Repository ISTITUZIONALE

Simulations of Vertical Displacement Oscillatory Modes and Global Alfvén Eigenmodes in JET geometry

Original
Simulations of Vertical Displacement Oscillatory Modes and Global Alfvén Eigenmodes in JET geometry / Barberis, T., C Kim, C., Porcelli, F., Banerjee, D., Hawkes, N., Kazakov, Y., Liu, Y., Oliver, J., E Sharapov, S., Yolbarsop, A.. - In: NUCLEAR FUSION. - ISSN 0029-5515. - 64:12(2024). [10.1088/1741-4326/ad7ed2]

Availability:
This version is available at: 11583/2993203 since: 2024-10-09T09:42:54Z

Publisher:
IOP science

Published
DOI:10.1088/1741-4326/ad7ed2

Terms of use:

This article is made available under terms and conditions as specified in the corresponding bibliographic description in the repository

Publisher copyright

(Article begins on next page)

25 November 2026

nuclear fusion
IAEA

PAPER • OPEN ACCESS

Simulations of vertical displacement oscillatory modes and global Alfvén Eigenmodes in JET geometry

To cite this article: T. Barberis *et al* 2024 *Nucl. Fusion* **64** 126064

View the article online for updates and enhancements.

You may also like

- Error field predictability and consequences for ITER
M. Pharr, N.C. Logan, C. Paz-Soldan et al.
- Invariant regimes of Spencer scaling law for magnetic compression of rotating FRC plasma
Yiming Ma, Ping Zhu, Bo Rao et al.
- An integral approach to plasma-wall interaction modelling for EU-DEMO
D. Matveev, C. Baumann, J. Romazanov et al.

This content was downloaded from IP address 130.192.43.106 on 10/12/2024 at 09:02

OPEN ACCESS
IOP Publishing | International Atomic Energy Agency
Nuclear Fusion
Nucl. Fusion **64** (2024) 126064 (14pp)
https://doi.org/10.1088/1741-4326/ad7ed2

Simulations of vertical displacement oscillatory modes and global Alfvén Eigenmodes in JET geometry

T. Barberis[1,2,*], C.C. Kim[3], F. Porcelli[1,7,*], D. Banerjee[1], N. Hawkes[4], Ye O. Kazakov[5], Y.Q. Liu[6], H.J.C. Oliver[4], S.E. Sharapov[4], A. Yolbarsop[7], NIMROD Team[a] and JET Contributors[b]

[1] Department of Applied Science and Technology, Polytechnic University of Turin, Torino 10129, Italy
[2] Princeton Plasma Physics Laboratory, Princeton University, Princeton, NJ 08543, United States of America
[3] SLS2 Consulting, San Diego, CA 92107, United States of America
[4] United Kingdom Atomic Energy Authority, Culham Science Centre, Abingdon, Oxfordshire OX14 3DB, United Kingdom of Great Britain and Northern Ireland
[5] Laboratory for Plasma Physics,LPP-ERM/ KMS,TEC Partner, Brussels, Belgium
[6] General Atomics, PO Box 85608, San Diego, CA 92186-5608, United States of America
[7] School of Nuclear Science and Technology, University of Science and Technology of China, Hefei, Anhui 230022, China

E-mail: tommaso.barberis@polito.it and francesco.porcelli@polito.it

Received 7 March 2024, revised 5 August 2024
Accepted for publication 24 September 2024
Published 4 November 2024



Abstract

Vertical Displacement Oscillatory Modes (VDOM), with frequency in the Alfvén range, are natural modes of oscillation of magnetically confined laboratory plasmas with elongated cross-section. These axisymmetric modes arise from the interaction between the plasma current, which is in equilibrium with currents flowing in external coils, and perturbed currents induced on a nearby conducting wall. The restoring force exerted by these perturbed currents on the vertical motion of the plasma column leads to its oscillatory behavior. An analytic model for VDOM was proposed by (Barberis *et al* 2022 *J. Plasma Phys.* **88** 905880511) based on an idealized 'straight tokamak' equilibrium with uniform equilibrium current density. This article introduces the first numerical simulations of VDOM in a realistic JET tokamak configuration, using the extended-MHD code NIMROD and drawing comparisons with Global Alfvén Eigenmodes (GAE). The results show qualitative agreement with analytic predictions regarding mode frequency and radial structure, supporting the identification of VDOM as a fundamental oscillation mode in tokamak plasmas. VDOM and GAE are modeled in a representative JET discharge, where axisymmetric perturbations with toroidal mode number $n = 0$ driven unstable by fast ions were observed. The two modes are examined separately using a forced oscillator within the NIMROD code, which enables a comparison of their characteristics and helps identify the experimentally observed mode possibly as a GAE.

[a] www.nimrodteam.org.
[b] See Maggi *et al* 2024 (https://doi.org/10.1088/1741-4326/ad3e16) for JET Contributors.
[*] Authors to whom any correspondence should be addressed.



Original Content from this work may be used under the terms of the Creative Commons Attribution 4.0 licence. Any further distribution of this work must maintain attribution to the author(s) and the title of the work, journal citation and DOI.

 © 2024 The Author(s). Published by IOP Publishing Ltd on behalf of the IAEA

Keywords: MHD waves, numerical simulation of MHD modes,
axisymmetric modes in toroidally confined plasmas, tokamak vertical stability

(Some figures may appear in colour only in the online journal)

1. Introduction

Tokamak plasmas with non-circular cross sections are known to be prone to an instability involving axisymmetric modes with toroidal mode number $n = 0$, which, if uncontrolled, can result in Vertical Displacement Events (VDE) and plasma current disruptions [1, 2]. Passive feedback stabilization can be achieved by using a nearby wall and plasma-facing components, as demonstrated in the original work by Laval *et al* [3]. The appropriate dispersion relation for the realistic case of a resistive wall surrounding the plasma is cubic [4, 5]. Two roots correspond to stable, weakly damped oscillations, with a frequency near the poloidal Alfvén frequency and a damping rate of the order of the inverse of the resistive wall time. The third one requires active feedback stabilization to be completely suppressed [6–9] as it would otherwise grow on the resistive wall time [4, 10–16] (or even faster, with a time proportional to a fractional power of wall resistivity when the condition of ideal MHD marginal stability is satisfied [17]).

Recent analytic work focused on the oscillatory solutions of the cubic dispersion relation, which were referred to as Vertical Displacement Oscillatory Modes (VDOM) [5]. This work was motivated by the observation of high frequency $n = 0$ modes in JET [18, 19], with frequency in the Alfvén range. In [18], it was proposed that the observed $n = 0$ modes were Global Alfvén Eigenmodes (GAE) [20] driven unstable by their resonant interaction with energetic ions, having energies in the MeV range, produced by auxiliary heating (combined NBI and ICRH) or by fusion reactions. While GAE remain a distinct possibility for the interpretation of the mentioned JET observations, it was pointed out in [5, 21] that an alternative possibility exists, as VDOM also oscillate in the Alfvén frequency range and therefore may also interact with fast ion orbits. GAE and VDOM are two different types of normal modes of a magnetically confined plasma, the former being internal modes, which can exist for different values of the toroidal mode number n, with frequency close to the minimum of the Alfvén continuum spectrum, while the latter are $n = 0$ external modes interacting with currents induced on the wall of the confining vacuum chamber by the vertical motion of the plasma. Other differences between the two modes involve their different spatial structure and their different sensitivity to details of safety factor q profile, plasma ellipticity, and plasma-wall distance. Given the apparent ease with which these modes can be destabilized by fusion alpha particles, both VDOM and GAE are likely to play an important role in future tokamak experiments where burning fusion plasmas will be produced.

This article aims to contribute to a more realistic assessment of the nature of VDOM, whose theoretical understanding is at present less developed than that of GAE. Indeed, VDOM were studied in [5, 21] using analytic theory within the framework of very simplified plasma models. In particular, small perturbations of a straight tokamak equilibrium were considered; both the equilibrium current density and plasma density profiles were assumed to be uniform in space up to a convenient elliptical flux surface, representing the plasma boundary, and going abruptly to zero beyond that boundary. Furthermore, the assumption of a uniform current density, or equivalently of a constant q profile, excluded the possibility of describing VDOM together with GAE in the simplified analytic model, as the Alfvén continuum spectrum can be expected to play no role for a constant q. The analytic work of [5, 21] also neglected possible effects related to plasma triangularity (in addition to ellipticity), as well as up-down asymmetry, as in the case of a single-null divertor configuration (up-down symmetry requires double-null), and the possible role of a halo plasma in the open field line region beyond the magnetic separatrix.

The analytic results reported in [5] were verified numerically in [22] using the extended-MHD NIMROD code [23], adopting the same idealized equilibrium configuration assumed in analytic work. This successful comparison between analytic theory and numerical results provided a useful benchmark and a solid starting point for the more realistic toroidal simulations presented in this article.

We consider here a representative JET discharge, shot #102371, where $n = 0$ modes were observed as shown by figure 1. This discharge accelerated neutral beam injected ions with third harmonic ion cyclotron resonance heating up to MeV energies. The power waveforms of the NBI and ICRH are shown in figure 2, along with other important plasma parameters. The plasma was heated with 6 MW of neutral beam injection, which began at 8 s. From 9 s, the ICRH power ramped up to 5 MW. The acceleration of the beam ions up to MeV energies increased the neutron yield by an order of magnitude. The plasma density increased from 8 s as the D beam injection fuels the plasma, as the line integrated electron density timetrace demonstrates. The discharge used a magnetic field of 2.3 T at the magnetic axis and a plasma current of 2 MA. The measured temperature shown in figure 2 indicates the presence of sawtooth activity.

As illustrated in figure 1, the $n = 0$ activity is associated with sawtooth crashes, and the modes seem to be driven during the first part of the sawtooth ramp following the crash. This behavior is linked to a significant feature of $n = 0$ perturbations, affecting both Vertical Displacement Oscillatory Modes (VDOM) and GAE. To destabilize an $n = 0$ perturbation through wave-particle interaction, the distribution

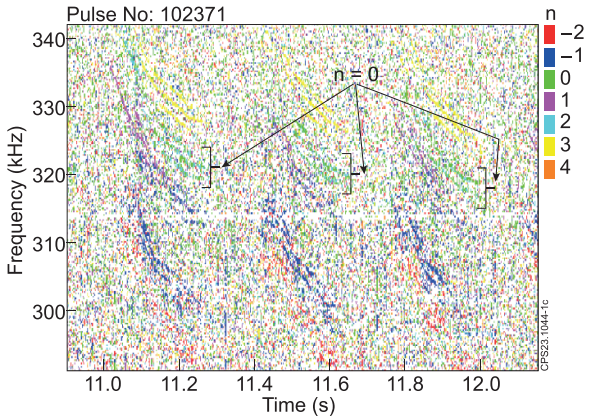


Figure 1. Phase magnetic spectrogram showing toroidal numbers of the modes excited in JET pulse #102371.

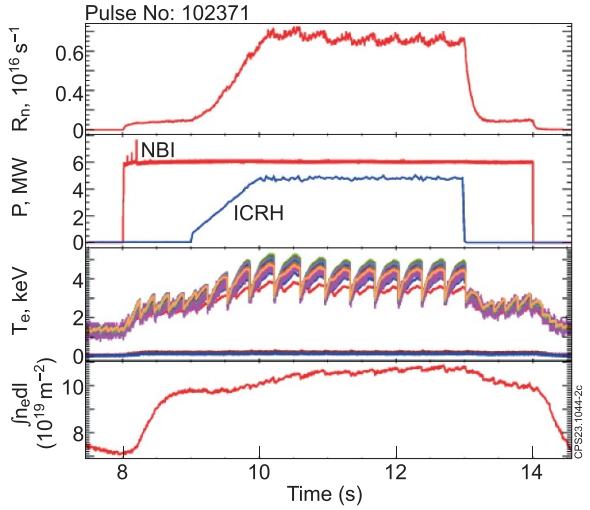


Figure 2. From top to bottom: temporal evolution of DD neutron rate; NBI and ICRH power waveforms; electron temperature measured by multi-channel ECE at different radii; line-integrated electron density measured with interferometer with the vertical line-of-sight through the magnetic axis in JET pulse #102371.

function of the energetic particles must exhibit a positive energy gradient, as described in [19, 21], or a significant anisotropy in velocity space. As suggested in [19] and further elaborated in [24], sawtooth crashes occurring on timescales shorter than, or comparable with the slowing down time of fast ions may result in a distribution function with $\partial F/\partial E > 0$. This mechanism is analogous to the one discussed for NBI blips in DIII-D [25].

We point out that our goal here is to present for the first time the characteristic signatures of VDOM as they appear in a numerical simulation of a realistic tokamak geometry, rather than to provide detailed modelling of a set of JET discharges, which will be the subject of a future publication. Our simulation indicates that two $n = 0$ oscillatory modes with Alfvénic frequencies can be found. Among these modes, identified as a VDOM and a GAE, the latter has a frequency comparable to the experimentally observed mode. Therefore we are led to identify the $n = 0$ oscillation of figure 1 as a GAE. Also, no attempt is made in this article to include in the numerical simulations the fast ion drive for either VDOM or GAE. Work is in progress to extend the kinetic-MHD module in NIMROD to include the type of fast ion distribution functions that may be responsible for the destabilization of $n = 0$ modes as observed in JET experiments. Due to the fact that our modeling does not include the main physical drive, the simulated modes will be damped. In order to study their properties in our simulation framework, we minimize the possible damping mechanisms associated with dissipative effects, focusing only on the mode structure and frequency dependence rather than destabilization thresholds.

This article is organized as follows. In section 2, VDOM analytic results are briefly presented, and a comparison between VDOM and GAE is discussed. In section 3, the main characteristics of the NIMROD code and the general setup for NIMROD linear simulations are discussed. Following a carefully selected initial perturbation, oscillatory plasma behaviour is observed. Fast Fourier Transform techniques reveal the presence of two distinct $n = 0$ normal modes in the Alfvén frequency range. Based on these results, section 4 describes the resonant plasma response to driven oscillator perturbation that mimics an antenna. By sweeping the frequency of the oscillator, we excite and study separately the two modes without relying on special initial conditions. The two distinct modes found in section 3 are interpreted as VDOM and GAE. Conclusions are reported in section 5.

2. Summary of VDOM analytic results and comparison with GAE

In this section we briefly summarize for the sake of completeness the main results of the analytic theory of VDOM, as discussed in [5]. A comparison between VDOM and $n = 0$ GAE [18, 20] is presented at the end of the section.

Analytic work was carried out within the framework of the linearized, reduced ideal MHD model [26], in the low-beta (= plasma pressure/magnetic pressure) approximation, neglecting toroidal effects and assuming a resistive wall. An idealized, up-down symmetric straight tokamak equilibrium for a plasma with elliptical cross-section, uniform plasma and current densities dropping abruptly to zero (as step functions) at the elliptical plasma boundary, was adopted. The cross-section of the confining wall was also assumed to be an ellipse confocal to the elliptical plasma boundary. In the VDOM regime, where the wall is sufficiently close to the plasma boundary to provide passive feedback stabilization of vertical displacements on the ideal MHD time scale, magnetic X-points associated with the elongated plasma cross-section lie outside the confining vacuum chamber, and so X-point effects on $n = 0$ modes [27, 28] were disregarded in the analytic treatment of VDOM.

Under these circumstances, adopting elliptical coordinates, normal mode analysis reveals that the most interesting VDOM has a mode structure corresponding to mode numbers $n = 0$,

$m=1$, where m is the elliptical angle mode number. The VDOM parity and radial structure correspond to a rigid vertical shift of the plasma column, whereby 'rigid' refers to the property that the vertical flow radial profile has a nearly constant amplitude from the magnetic axis to the plasma edge. A return flow is concentrated in the region where the plasma density drops to zero, giving rise to a vorticity layer at the elliptical plasma boundary. We may expect that the mode structure will be less rigid for more realistic plasma and current density profiles, and that the return flow will involve a finite region close to the plasma edge.

With these simplifying assumptions, and assuming perturbations depending on time as $\exp(-\mathrm{i}\omega t)$, with $\omega=\mathrm{i}\gamma$ a complex eigenfrequency, a cubic dispersion relation for VDOM was derived in [5]:

$$\gamma^3+\frac{\gamma^2}{(1-\hat{e}_0 D)\,\tau_{\eta w}}+\gamma\gamma_\infty^2\frac{D-1}{1-\hat{e}_0 D}-\frac{\gamma_\infty^2}{(1-\hat{e}_0 D)\,\tau_{\eta w}}=0, \tag{1}$$

where $\tau_{\eta w}$ is the resistive wall time,

$$\gamma_\infty=\frac{2\kappa}{\kappa^2+1}\left(\frac{\kappa-1}{\kappa}\right)^{1/2}\tau_{\mathrm{A}}^{-1}, \tag{2}$$

is the ideal MHD growth rate of $n=0$ vertical displacements in the no-wall limit, the relevant Alfvén time is defined as $\tau_{\mathrm{A}}=(4\pi\varrho_m)^{1/2}/B_{\mathrm{p}}'$, with B_{p}' the on-axis radial derivative of the poloidal magnetic field, $\kappa=b/a$ is the elongation of the elliptical plasma boundary having a and b as minor and major semi-axes, respectively, $\hat{e}_0=e_0\kappa/(\kappa+1)$, and $e_0=(\kappa^2-1)/(\kappa^2+1)$ is the ellipticity of the plasma boundary. The geometric wall parameter, D, is defined as

$$D\left(\kappa,\frac{b}{b_{\mathrm{w}}}\right)=\frac{\kappa^2+1}{(\kappa-1)^2}\left\{1-\left[1-\frac{\kappa^2-1}{\kappa^2}\left(\frac{b}{b_{\mathrm{w}}}\right)^2\right]^{\frac{1}{2}}\right\}. \tag{3}$$

This parameter depends on the elongation, κ, and on the plasma-wall distance, represented by the parameter b/b_{w}, where b_{w} is the major semi-axis of the elliptical wall. Confocality between the plasma boundary and the wall implies that $b_{\mathrm{w}}^2-a_w^2=b^2-a^2$. In the no-wall limit, $b/b_{\mathrm{w}}\to 0$, D vanishes. When the wall touches the plasma boundary, $b/b_{\mathrm{w}}=1$ and D reaches its maximum value, which is always larger than unity. $D=1$ when the wall is at the critical distance from the plasma, corresponding to the condition of ideal MHD marginal stability for vertical displacements in the presence of passive feedback stabilization provided by a perfectly conducting wall. For the specific geometry assumed in the analytic treatment, it was found in [3, 17] that the ideal marginal stability condition, $D=1$, corresponds to the wall intercepting the X-points of this idealized, up-down symmetric double-null configuration. When $D>1$, the magnetic X-points lie outside of the vacuum chamber and the ideal MHD vertical mode is suppressed by passive wall stabilization.

If the wall is perfectly conducting, $\tau_{\eta w}\to\infty$, the dispersion relation reduces to a quadratic, with solutions:

$$\gamma^2=\frac{1-D}{1-\hat{e}_0 D}\gamma_\infty^2. \tag{4}$$

The VDOM regime corresponds to values of $D>1$, such that γ^2 is negative and

$$\omega=\pm\omega_0=\pm\left[\frac{D-1}{1-\hat{e}_0 D}\right]^{1/2}\gamma_\infty, \tag{5}$$

is a real quantity; ω_0 corresponds to the VDOM oscillation frequency. Inspection of equations (2), (3) and (5) reveals that the VDOM frequency depends mainly on the Alfvén time, scaling with $(B_{\mathrm{p}}'/\varrho_m)^{1/2}$, the elongation κ, and the plasma-wall distance b/b_{w}. An important consideration regarding the analytic dispersion relation is related to the parameter D. The analytic expression in equation (3) is only applicable for confocal elliptical plasma boundary and wall. Because the shape and relative distance of the wall greatly impact this geometrical parameter, our simplified model cannot provide a reliable pre-estimate of the value of D corresponding to the realistic JET wall shape. An important consequence is that, based on the simplified analytic model, ideal vertical stability ($D>1$) requires that the magnetic X-points lie outside the toroidal chamber. In contrast, the JET configuration explored in the subsequent sections features a single null, with one of the X-points located inside the toroidal chamber. Nevertheless, the stabilization of the ideal vertical instability, and hence the existence of VDOM, is ensured on JET, even when one X-point is inside the toroidal chamber, because the JET wall is on average closer to the plasma boundary than the analytic estimate based on a confocal wall.

The VDOM characteristic properties presented above have been obtained using a simplified straight tokamak equilibrium. The purpose of the present article is to verify whether these properties remain qualitatively true when a more realistic tokamak configuration is considered. Assuming that this will be the case, a comparison between VDOM and GAE can be presented. GAE are mainly internal modes, while VDOM are external modes. The GAE radial structure is such that the perturbed poloidal flow peaks near the minimum of the $n=0$ continuum spectrum, while the VDOM radial structure is largely insensitive to the q profile. Both modes are global, but with a different parity with respect to the poloidal angle. The GAE perturbed flow has an even parity, corresponding to a side-to-side motion of the plasma core along the equatorial plane of the toroidal configuration. The VDOM perturbed flow has an odd parity, corresponding to a nearly rigid-shift, up-down vertical motion of the plasma core. Both GAE and VDOM frequencies scale as the inverse of the Alfvén time, i.e. $\omega\propto(B_{\mathrm{p}}'/\varrho_m)^{1/2}$. The GAE frequency is close to the minimum of the $n=0$ continuum spectrum, which depends on the q profile, and only weakly depends on plasma-wall distance. By contrast, the VDOM frequency depends on plasma-wall distance, while it is largely insensitive to details of the q profile. This comparison between GAE and VDOM is summarized in table 1.

Table 1. Comparison between VDOM and GAE.

VDOM	GAE
• External mode.	• Internal mode.
• Global, odd parity with respect to poloidal angle.	• Global, even parity with respect to poloidal angle.
• Nearly rigid shift, up-down vertical motion, radial structure weakly dependent on q profile.	• Poloidal flow peaking near minimum of $n=0$ Alfvén continuum, radial structure depends on q profile.
• Alfvénic frequency dependent on plasma elongation and plasma-wall distance, weakly dependent on q profile details.	• Alfvénic frequency close to the minimum of the $n=0$ Alfvén continuum.

If finite wall resistivity is retained, then, in the relevant limit $\omega_0\tau_{\eta w} >> 1$, VDOM oscillations are weakly damped, with a damping rate of the order of the inverse resistive wall time (except at ideal MHD marginal stability, $D=1$, where the damping rate is stronger, scaling with a fractional power of resistivity [17]). A third root with zero oscillation frequency can be obtained from equation (1), which corresponds to a purely growing solution reaching a finite amplitude on the resistive wall time scale. As mentioned in the Introduction, this zero-frequency root could develop into a VDE and requires active feedback stabilization to be suppressed. A discussion of this zero-frequency solution is outside the scope of this article.

3. Linear simulations with NIMROD [23]

The simulations described in this article advance the linearized version of the standard non-linear single-fluid resistive MHD equations (6)–(9) in toroidal geometry using the 3D initial value code NIMROD:

$$\frac{\partial n}{\partial t} + \nabla\cdot(n\mathbf{v}) = \nabla\cdot\mathcal{D}\nabla n \tag{6}$$

$$mn\left(\frac{\partial}{\partial t} + \mathbf{v}\cdot\nabla\right)\mathbf{v} = \frac{1}{\mu_0}(\nabla\times\mathbf{B})\times\mathbf{B} - \nabla p + \nabla\cdot\nu\rho\nabla\mathbf{v} \tag{7}$$

$$\frac{\partial}{\partial t}p + \mathbf{v}\cdot\nabla p = -\Gamma p\nabla\cdot\mathbf{v} \tag{8}$$

$$\frac{\partial\mathbf{B}}{\partial t} = -\nabla\times[\eta_e(\nabla\times\mathbf{B}) - \mathbf{v}\times\mathbf{B}] + \kappa_{\mathrm{divb}}\nabla\nabla\cdot\mathbf{B}. \tag{9}$$

In these equations, n and m are respectively particle density and ion mass. The total pressure of electrons and ions is p, $\mathbf{v}$ is the center-of-mass plasma velocity, $\Gamma = 5/3$ is the adiabatic coefficient used in the adiabatic heat flux closure and $\mathbf{B}$ is the magnetic field. Explicit diffusive terms are included in the model: the density diffusivity $\mathcal{D}$, kinetic viscosity ν, electrical diffusivity coefficient η_e (= resistivity over the vacuum permeability μ_0), and κ_{divb} is a diffusivity coefficient used to control the $\nabla\cdot\mathbf{B}$ error in the induction equation. The code employs high-order quadrilateral finite elements for modelling the poloidal plane and pseudo-spectral techniques for the periodic axisymmetric direction. NIMROD can efficiently advance both linear and nonlinear extended-MHD equations, with implicit or semi-implicit time-advance methods to address the temporal stiffness associated with multiple time scales. For this study, we utilized only the linearized model implementation to evolve the $n = 0$ toroidal harmonic perturbation.

The results presented in the following sub-sections report linear NIMROD simulations using the EFIT [29, 30] reconstructed equilibrium of JET shot #102371 at time $t = 11.00$ s, which was constrained using polarimetry measurements. The equilibrium pressure and safety factor provided by EFIT are shown in figures 3(*a*) and (*b*), respectively. The profile are computed at a time during a sawtooth ramp, when the $n = 0$ activity is present. It should be noted that the q profile falls below unity. While the VDOM structure is expected to be largely insensitive to the q profile, the GAE dependence is restricted towards the edge close to the minimum of the Alfvén continuum. Thus, for both modes we do not expect strong effects due to the q profiles changes in the core due to sawtooth activity, which are not considered in the following.

Figure 3(*c*) shows our best fit of the equilibrium electron density profile. The on-axis value of the electron density is $n_0 = 5.2\times10^{19}$ m^{-3}. The experimentally measured value of the effective charge, $Z_{\mathrm{eff}} = 1.75$, was also used to evaluate the plasma mass density. The plasma in the open field line region is represented using a 'halo' plasma model, with low density and high resistivity. In particular, the plasma density profile is uniform in the open field line region with a value of $n_{\mathrm{halo}} = 5\times10^{17}$m^{-3}.

Although some level of dissipation is required to ensure the proper convergence of the numerical scheme, we do not attempt to simulate realistic tokamak dissipative parameters. Both resistivity and viscosity are assumed to be constant and are minimized inside the 'hot' region to mimic an ideal plasma. The primary reason for this procedure is the absence of the energetic particle drive, as discussed in the Introduction, which is necessary for the destabilization of both GAE and VDOM. The dissipative terms mainly influence the damping rate of the modes, but have less impact on the mode structure and frequency, which are the focus of this work.

In the following simulations, the grid resolution is (mx,my) = (60,90) with polynomial degree = 3 and the timestep $\Delta t = 10^{-7}$ s. The grid is flux aligned with 60 radial points and 90 points along the poloidal direction. More details on the finite element grid construction can be found in [23]. We used grid

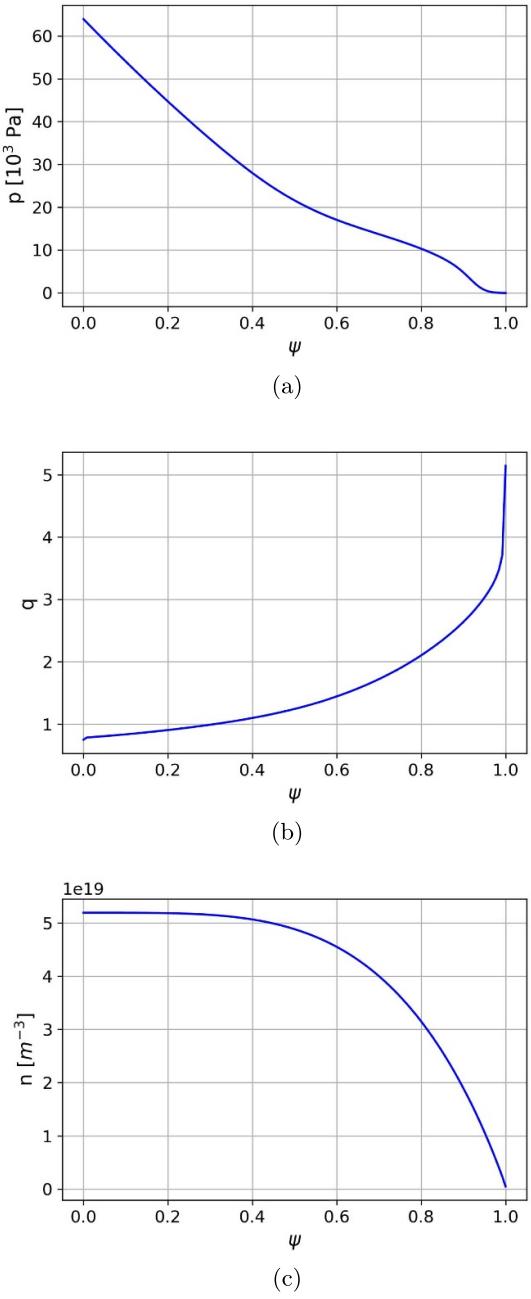


Figure 3. EFIT equilibrium pressure profile (*a*), and safety factor (*b*); best fit of the experimental electron density profile (*c*), as functions of normalized flux. The separatrix is at $\psi = 1$.

point packing for improved numerical convergence at the X-point region and close to the plasma boundary, at which the resistivity value jumps from the nearly ideal value in the 'hot' plasma to the high resistivity of the halo region. The relative low value of the timestep is required in order to properly resolve the Alfvénic oscillatory modes.

The simulation boundary is assumed to be an ideal conducting wall. In NIMROD, the ideal conducting wall is implemented with vanishing normal components of the perturbed magnetic field at the simulation boundary. In some of our simulations, we have used the actual shape of the JET wall. However,

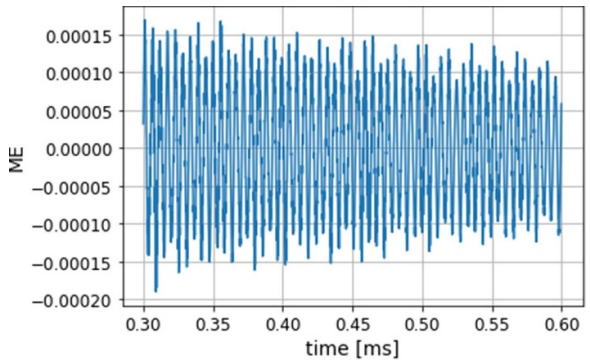


Figure 4. Oscillatory behaviour of the magnetic energy in response to a 'vertical push', in the time interval between $t = 0.3$ ms and $t = 0.6$ ms.

most cases use a simplified wall where the wall is located at a constant distance, δ_W, from the plasma separatrix. The two types of wall shapes used yield similar simulation results (see section 3.1. below).

The simulations presented in this section describe the plasma response to an initial perturbation in velocity corresponding to a rigid vertical shift of the plasma, dubbed 'vertical push' in the following. The oscillatory behaviour of all relevant perturbed fields follows the initial vertical push. Figure 4 shows the behaviour of the magnetic energy as a function of time. Weak damping of the oscillatory behaviour is observed. The careful choice of initial perturbation is necessary, because VDOM are stable modes, and therefore different initial conditions lead to a mix of different oscillatory modes. The resulting interference would cause a rapid decay of all modes, including the VDOM. This problem is overcome in the next section, where a different method to drive the perturbation is examined.

Figure 5 shows contour plots of tangential and normal components, with respect to the equilibrium flux surfaces, of the perturbed magnetic field. Figure 6 shows the contour plots of perturbed pressure. Both plots are taken at time $t = 0.5$ ms in the simulation, corresponding to a minimum of the magnetic energy oscillation (the last time shown in figure 4). An $m = 1$ mode structure is evident in the perturbed fields; the pressure perturbation shows the up-down feature characteristic of VDOM.

Fast Fourier Transform (FFT) has been employed to analyze the temporal behaviour of the plasma response. The whole linear simulation time of 1 ms has been considered to compute the discrete Fourier Transform (DFT) with the efficient FFT algorithm [31]. The FFT signal of the magnetic energy time trace is shown in figure 7. A dominant peak in the FFT signal can be identified at frequency $f_{low} = 184$ kHz, while a secondary peak indicates the presence of a second subdominant mode at frequency $f_{high} = 311$ kHz. This indicates the presence of two Alfvén-frequency normal modes with $n = 0$ that are both excited in response to the initial vertical push. The simultaneous presence of the two modes gives rise to interference. The space and time dependence of the plasma response cannot be separated in this case. As the two modes are damped in time

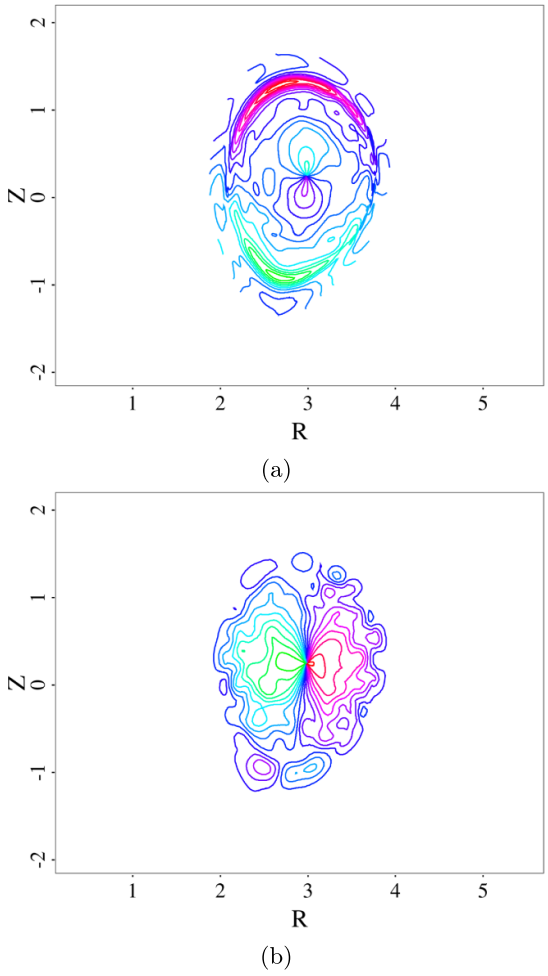


Figure 5. Magnetic field perturbation in response to a 'vertical push'. (*a*) Tangential, and (*b*) normal B-components with respect to the equilibrium flux surfaces. A main $m=1$ structure, expected for the VDOM, can be identified.

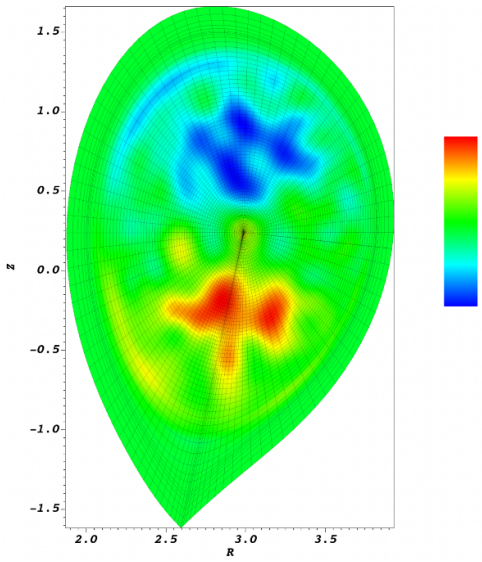


Figure 6. Pressure perturbation, $\tilde{p}$, in response to a 'vertical push', showing the up-down structure characteristic of the VDOM. Overlayed is displayed the grid showing the radial grid point packing at the plasma boundary and poloidal angle grid point packing at the X-point.

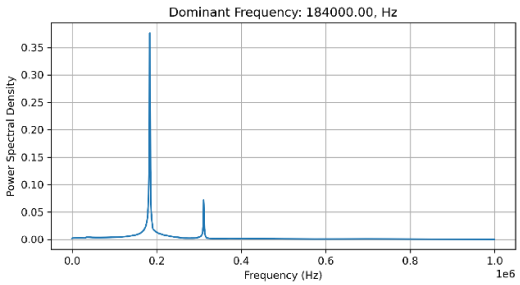


Figure 7. FFT signal (absolute value) of the oscillating magnetic energy in simulation ('vertical push'). Two peaks can be identified: a dominant one at 184 kHz, and a secondary one at 311 kHz.

at different rates, the contour plots of figures 5 and 6 change in time, and the coherent mode structure is lost.

3.1. Wall position scan

In the following, scans of the wall position and of the density profiles reveal similarities and different behaviours of the two modes.

As discussed in section 2, the VDOM frequency depends on the distance between the plasma and the wall, while the GAE frequency does not. A scan of the wall position highlights the different behaviour of the two modes. The frequency as a function of the distance between the separatrix and the wall, δ_W, is plotted in figure 8. As the wall is pushed further away from the plasma boundary to $\delta_W \approx 0.23$ m, the frequency of the higher-frequency mode is almost unaffected, while the frequency of the lower-frequency mode changes by more than 10%, its oscillation frequency varying from 189 kHz to 170 kHz. The actual shape of the JET wall in the simulation yields equivalent results to the simplified wall at a plasma-wall distance $\delta_W \approx 0.11$ m, as indicated in figure 8(*a*) by the green line, representing the actual wall results.

The wall scan suggests that the higher-frequency mode is a GAE, while the lower-frequency mode is a VDOM. However, further analysis is needed before this conclusion can be confirmed. In the scenario where the wall position matches the plasma boundary ($\delta_W = 0$), the theoretical model outlined in section 2 predicts an infinite frequency for the VDOM, with the displacement reducing to zero due to the absence of a vacuum region allowing for rigid plasma oscillations. On the other hand, our simulation reveals a somewhat different, albeit not completely unexpected behavior. As shown in the following sections, the realistic geometry leads to a mode structure that is rigid-like only in a more core-localized area. When the wall closes in on the plasma boundary, causing the vacuum region to shrink, the compressed plasma against the ideal wall induces a return flow not only in the halo plasma but also

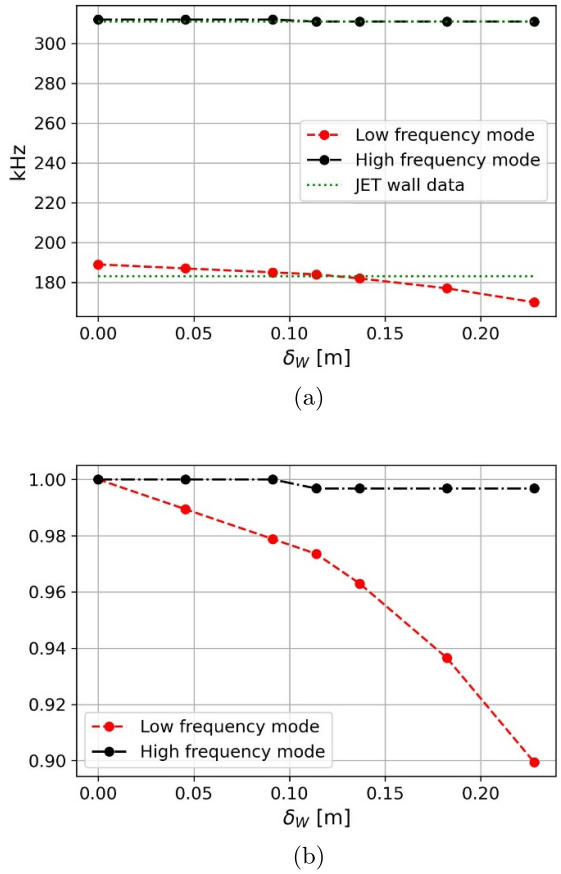


Figure 8. Frequency of high and low frequency modes as function δ_W. The dashed green line in (*a*) corresponds to the actual JET wall distance and shape. (*b*) Plots the two frequencies normalized to their maximum values, indicating percentage variations.

within the hot plasma region. When the plasma boundary and wall coincide, the mode retains some VDOM characteristics. However, this return flow becomes strongly localized in the hot plasma region, leading to an edge perturbation with an amplitude comparable with the main rigid-like structure in the core.

3.2. Density profile scan

The frequency of Alfvén modes scales as the inverse of the square root of the plasma density. Here, we consider the effect of changing the density profile in NIMROD simulations, effectively changing the volume-averaged plasma density. Figure 9 illustrates the various density profiles considered in the density scan. Throughout all profiles, the on-axis and halo region density values are kept constant at $n_0 = 5.2 \times 10^{19}$ and $n_{\rm halo} = 5.0 \times 10^{17}$. The profiles follow $n(\psi) = (n_0 - n_{\rm halo})(1 - \psi^{p_1})^{p_2} + n_{\rm halo}$. By adjusting the parameter p_1 while keeping $p_2 = 0.96$ constant, we vary the volume-averaged density.

Figure 10 shows that the frequency of the two $n = 0$ modes follows the same decreasing trend with increasing density. As represented in figure 10(*b*), the normalized frequency is

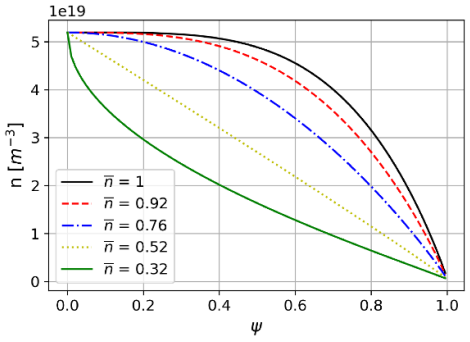


Figure 9. Density profiles as functions of normalized flux. Each profile is associated to its volume averaged value, $\overline{n}$, normalized to the one of the experimental best fit (solid black curve, same as in figure 3(*c*)).

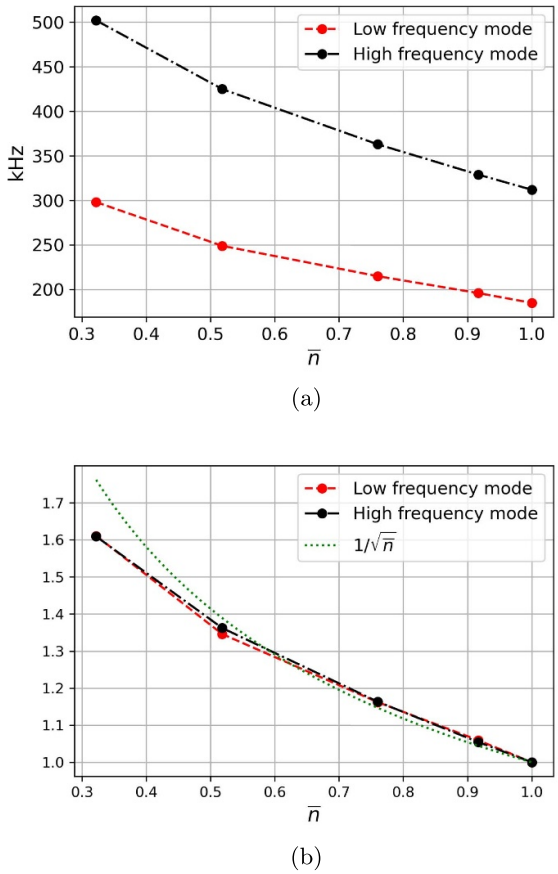


Figure 10. Frequency of high and low frequency modes as a function of the normalized volume averaged density, $\overline{n}$: (*a*) plots the two frequencies in kHz; (*b*) plots the two frequencies normalized to their values at $\overline{n} = 1$; the $1/\sqrt{n}$ dependence is shown by the dashed green line.

proportional to $1/\sqrt{n}$, as expected for Alfvénic oscillations. It should be noted that the profile will likely have an effect in determining the extent of the rigid-like structure of the VDOM. However, further exploration of this is beyond the scope of the present manuscript.

4. Driven oscillator perturbation

To study the two oscillatory modes found in section 3 separately, an alternate perturbation is implemented in the NIMROD code. Instead of an initial 'vertical push', the temperature evolution equation has been modified to include a time-dependent oscillatory term:

$$\frac{3}{2}\left(\frac{\partial}{\partial t}+\mathbf{v}\cdot\nabla\right)T=-T\nabla\cdot\mathbf{v}+A\sin\left(2\pi f_0 t\right)\times\exp\left[\frac{(r-r_0)^2+(z-z_0)^2}{\Delta_0^2}\right] \quad (10)$$

where f_0 is the driven oscillation frequency for the temperature, and A is the amplitude of the driving term. A Gaussian function with width Δ_0 localizes the oscillator perturbation in space around r_0, z_0 in the poloidal plane. This forced oscillation for the temperature mimics the injection of a wave from an external antenna. Scanning the oscillator frequency, it is then possible to look for resonances in the plasma response associated with plasma normal modes. All other fields have zero initial perturbation.

These simulations use $r_0 = 2.8$ m, $z_0 = 1.71$ m and $\Delta_0 = 0.5$ m. The oscillator is localized in the open field line region. This ensures that the driven mode structure remains independent of the oscillator's radial position and avoids any spurious contributions from the oscillator itself. The amplitude A determines the amplitude of the saturated normal modes.

4.1. Low frequency mode

With the same simulation parameter of section 3, we perform a scan in the oscillator frequency, f_0, in the neighborhood of the low frequency signal identified by FFT. Figure 11 shows the amplitude of the saturated oscillations for the normal component of the perturbed magnetic field, normalized to the off-resonance minimum amplitude value (blue dot at $f_0 = 190$ kHz). For values of f_0 close to 183 kHz, the saturated value increases by more than an order of magnitude. The mode frequency and damping can be evaluated assuming the following resonance condition for a generic quantity Y:

$$Y=\frac{C}{(\omega_0-\omega)-i\gamma} \quad (11)$$

where C is a constant, $\omega_0 = 2\pi f_0$, with ω_0 the frequency of the forcing term, ω is the frequency of the normal mode, and γ is its damping rate. The amplitude can be fitted by a Lorentzian function:

$$|Y|=\frac{C}{\sqrt{(\omega_0-\omega)^2+\gamma^2}} \quad (12)$$

where ω and γ are related to the peak and the width of the Lorentzian.

Figure 11 shows the resonance peak is found for mode frequency $f = 183.5$ kHz; the damping rate is $\gamma = -1240\,\mathrm{s}^{-1}$.

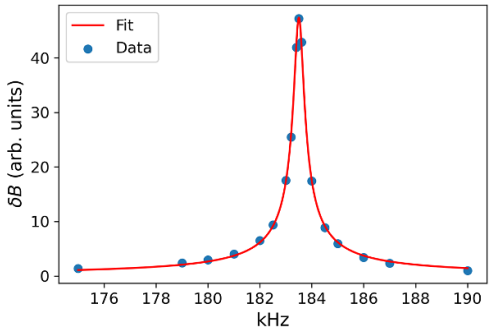


Figure 11. Normalized amplitude of the normal component of the perturbed magnetic field as a function of oscillator frequency f_0 in the neighbourhood of f_{low}. Blue dots, corresponding to numerical results, are fitted by the red curve assuming the resonant condition (12), with $\omega_0 = 1153 \times 10^3$, $\gamma = -1.240 \times 10^3$ and $C = 58.72$.

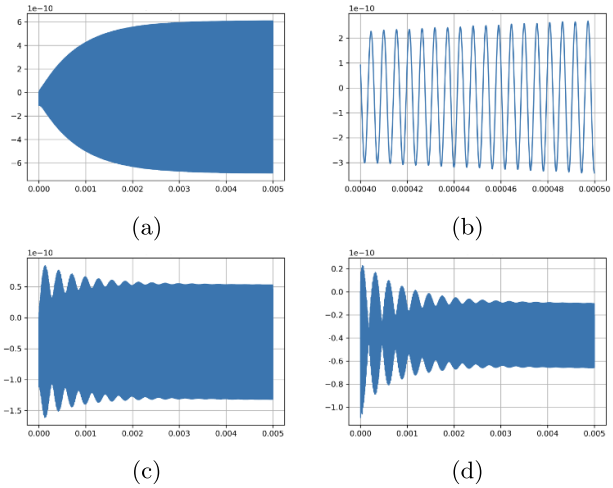


Figure 12. (*a*) Magnetic energy time trace for forced oscillator frequency at resonance, $f_0 = 183.5$ kHz; (*b*) same as in the previous panel, zoomed in the time interval between $t = 0.4$ ms and $t = 0.5$ ms. In (*a*) only the envelope of the fast oscillatory behaviour is evident, due to the time range of the plot. The envelope of the oscillatory behaviour of the magnetic energy is shown for off-resonant frequencies of the forced oscillator in (*c*) for $f_0 = 180$ kHz and (*d*) for $f_0 = 187$ kHz.

The frequency corresponds to the main peak of the FFT signal in figure 7.

Figure 12 shows the time traces of the magnetic energy for resonant and off-resonant oscillator frequencies, respectively. When the oscillator resonates with the mode, a growing oscillatory pattern is obtained. The envelope of the oscillation initially grows and then saturates in time at $t > 4.0$ ms. For the off-resonant cases, we observe a clear beating between the oscillator frequency f_0 and the mode frequency f, with beating frequency $f_b = |f - f_0|$. For $t > 4.0$ ms, the beating dies away, leaving only a constant amplitude oscillation at the forcing frequency f_0.

The level of dissipation in the system affects the damping of the mode, and consequently, it determines the width and the amplitude of the resonant peak in the plasma response, as shown in figure 13. An increase of the viscosity parameter by

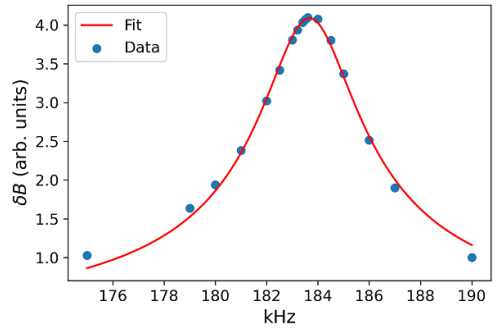


Figure 13. Same as in figure 11, but for a viscosity value 20 times larger.

20 times leads to a damping rate $\gamma = -11.8 \times 10^3\,\mathrm{s}^{-1}$. For this case, the fitting parameters for equation (12) are: $\omega_0 = 1154 \times 10^3$, $\gamma = -11.79 \times 10^3$ and $C = 48.20$, showing a γ increase of approximately 10 times.

Selecting carefully the oscillator perturbation frequency f_0 it is then possible to study separately the structure of the two modes found in section 3. This requires the forced oscillator frequency to be resonant with the mode, i.e. close to the peak described by the fitting Lorentzian of equation (12), thus maximizing the plasma response. Under these conditions, choosing $f_0 = 183.5$ kHz for the low frequency mode, a $m = 1$ mode structure in the magnetic perturbation develops, and an up-down symmetric perturbation in pressure is established, as shown in figures 14 and 15, which are characteristic of the VDOM described in section 2. The mode structure appears to be more core localized with respect to the theoretical description, because both plasma density and current density profiles used in the simulations are peaked, while analytic theory assumed flat profiles for the sake of simplicity.

Finally, the perturbed velocity vector plot of figure 16 shows a nearly rigid vertical plasma displacement in the region where the mode is localized.

To analyze the structure of the low frequency mode in more detail, figure 17 plots the perturbed momentum in the vertical direction along horizontal and vertical slices; from the magnetic axis to the plasma edge. The normalized distances along these slices are denoted by x and y in the figure. Along the horizontal slice, the perturbed momentum is the poloidal flow multiplied by the plasma density, $n\tilde{V}_\theta$. The perturbed momentum exhibits a nearly rigid shift structure in the core region, changing sign as the plasma edge is approached. In analytic theory, as discussed in section 2, the return flow is a thin layer localized at the plasma boundary, as a consequence of the step-function profiles for plasma mass and current densities and of the incompressibility of the perturbation $\nabla \cdot \boldsymbol{v} = 0$. In our simulations, the return flow exhibits a finite spatial extent inside the plasma. This behavior is consistent with the condition $\nabla \cdot \boldsymbol{v} = 0$. The region in which the return flow propagates is affected by the finite gradient of the density profile in the plasma, deviating from the assumption of a uniform profile of the theoretical model. A more in-depth analysis of this

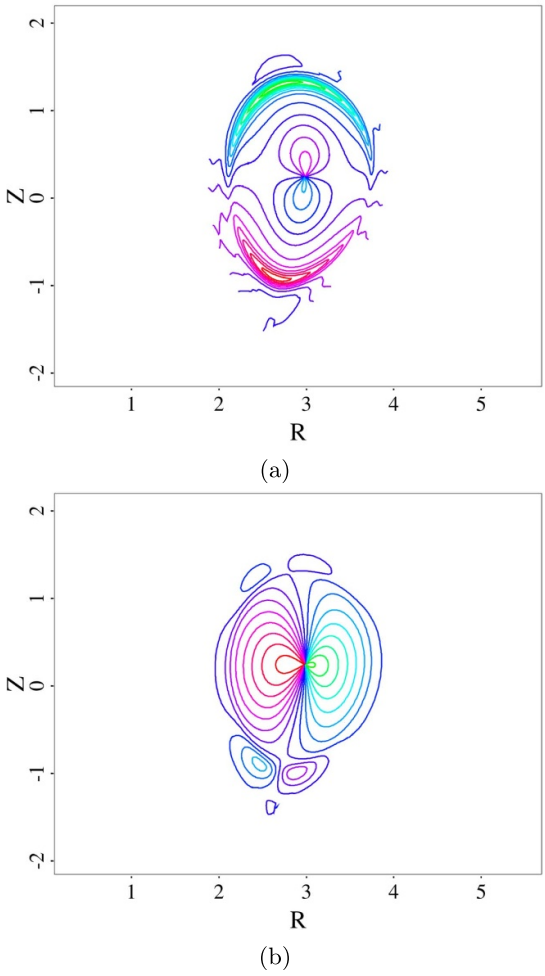


Figure 14. Perturbed magnetic field components at $t = 4.4$ ms for forced oscillator frequency at resonance, $f_0 = 183.5$ kHz. (*a*) Tangential, and (*b*) normal B-components with respect to the equilibrium flux surfaces.

feature is planned for a future publication. Along the vertical slice, figure 17(*b*), the vertical component of the perturbed momentum is the radial flow multiplied by the plasma density, $n_0\tilde{V}_r$, which is nearly constant in the plasma core and decreases monotonically to zero at the plasma edge.

The mode structure obtained for the low frequency mode exhibits the important characteristics associated with the VDOM, as highlighted in table 1. The non-uniform plasma and current density profiles considered in the numerical simulation have an important impact on the mode structure. However, a global, nearly rigid shift structure is maintained in the plasma core, while a return flow is localized around the plasma edge. The lower mode frequency depends on the plasma-wall distance, as shown by figure 8, and scales inversely with the square root of the plasma density, as shown by figure 10. These results allow us to conclude that the low-frequency mode is indeed a Vertical Displacement Oscillatory Mode. This is the first time that the VDOM is identified in a simulation using realistic tokamak geometry.

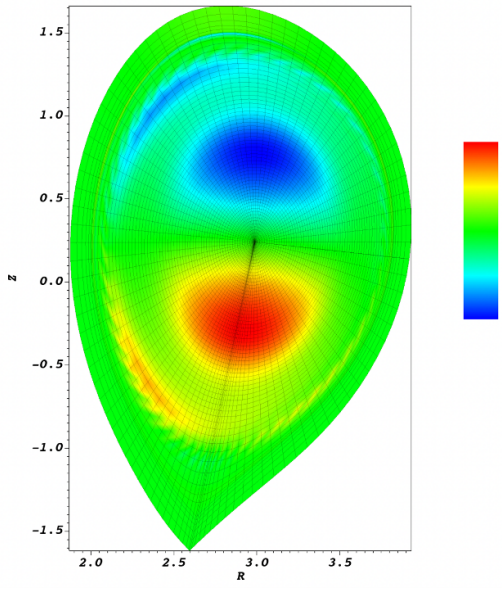


Figure 15. Perturbed pressure at $t = 4.4$ ms for forced oscillator frequency at resonance, $f_0 = 183.5$ kHz. Overlayed is displayed the grid showing the radial grid point packing at the plasma boundary and poloidal angle grid point packing at the X-point.

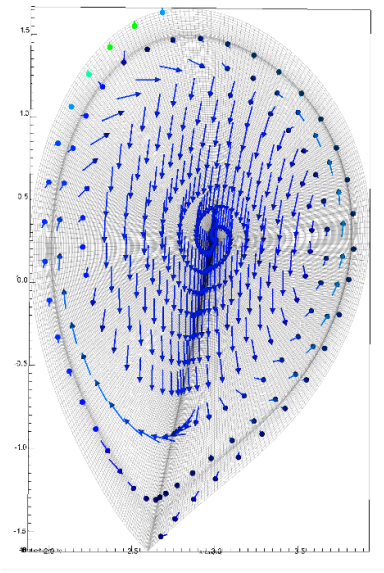


Figure 16. Vector plot of $\tilde{\mathbf{v}}$ at $t = 4.4$ ms for forced oscillator frequency at resonance, $f_0 = 183.5$ kHz.

4.2. High frequency mode

The same analysis is now repeated for the higher-frequency mode, scanning the forced oscillator frequency in the neighbourhood of f_{high}. Figure 18 shows the amplitude of the saturated oscillations for the normal component of the perturbed magnetic field, normalized to the off-resonance minimum amplitude value (blue dot at $f_0 = 320$ kHz). A resonance is found at the frequency obtained by the FFT analysis of the plasma response following a 'vertical push'. The fit of the resonance condition equation (12) reveals a resonant frequency $f = 311.4$ kHz and a mode damping rate $\gamma = -1060\,\text{s}^{-1}$.

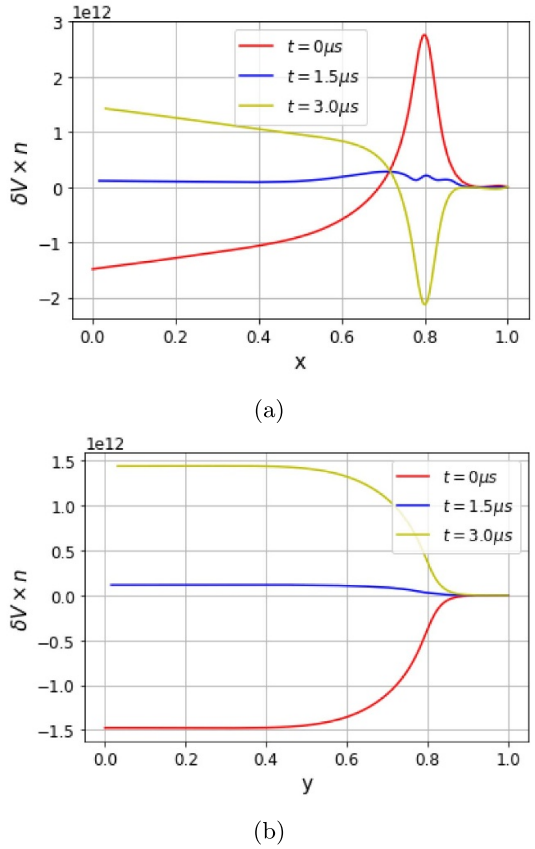


Figure 17. Vertical component of the perturbed momentum, plotted in (*a*) along a horizontal slice, and in (*b*) along a vertical slice, for different times during one oscillation.

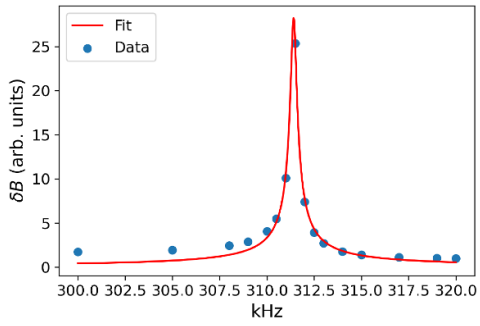


Figure 18. Normalized amplitude of the normal component of the perturbed magnetic field as a function of oscillator frequency f_0 in the neighbourhood of f_{high}. Blue dots, corresponding to numerical results, are fitted by the red curve, assuming the resonant condition (12).

The mode structure near resonance ($f_0 = 311.5$ kHz) is shown in figures 19 and 20. The higher frequency mode presents an orthogonal mode parity with respect to the lower frequency one. The vector plot of figure 21 shows a perturbed flow, oscillating inward and outward along the equatorial midplane, localized in the plasma core, together with a return poloidal flow in the outer region of the plasma. In figure 22, 1D plots of the horizontal component of the perturbed momentum

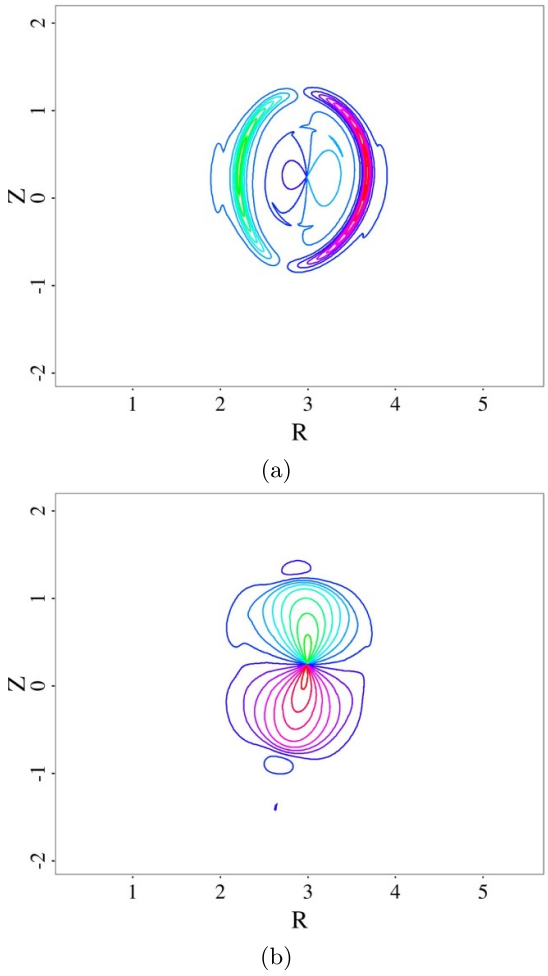


Figure 19. Perturbed magnetic field components at $t = 4.5$ ms for forced oscillator frequency at resonance, $f_0 = 311.5$ kHz. (*a*) Tangential, and (*b*) normal B-components with respect to the equilibrium flux surfaces.

along horizontal and vertical slices are shown. The mode structure is global with a strong peak of the poloidal flow, $\tilde{V}_\theta$, close to the plasma edge. This peak is located close to the minimum of the $n = 0$ Alfvén continuum, and the frequency value at the minimum of the spectrum compares well with the one obtained for the mode.

These features are characteristic of the $n = 0$ GAE, as described in table 1, leading to the identification of the high-frequency mode in our NIMROD simulation as a GAE.

5. Conclusions

We have presented the first numerical simulations of Vertical Displacement Oscillatory Modes (VDOM) in realistic tokamak geometry. The numerically resolved characteristics of VDOM are in very good qualitative agreement with those found previously by analytic work based on an idealized straight tokamak equilibrium. These simulations provide conclusive evidence that VDOM are natural modes of oscillations of tokamak plasmas. These modes are damped by wall resistivity and by plasma collisional processes such as viscosity.

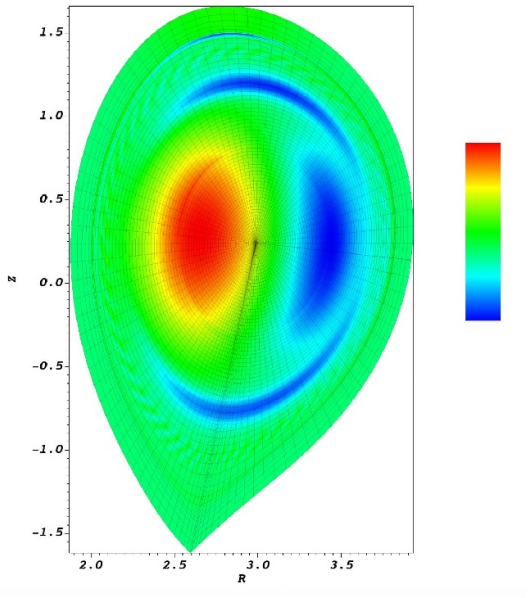


Figure 20. Perturbed pressure at $t = 4.5$ ms for forced oscillator frequency at resonance, $f_0 = 311.5$ kHz. Overlayed is displayed the grid showing the radial grid point packing at the plasma boundary and poloidal angle grid point packing at the X-point.

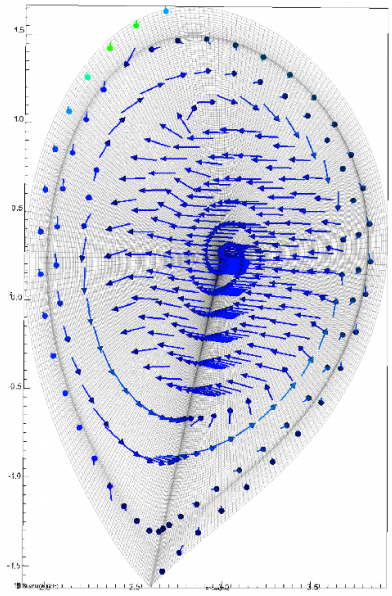


Figure 21. Vector plot of the perturbed velocity $\tilde{\mathbf{v}}$ at $t = 4.5$ ms for forced oscillator frequency at resonance, $f_0 = 311.5$ kHz.

Therefore, they are not typically observed in tokamak experiments under normal operation conditions, but may be driven unstable by MeV fast ions, as suggested in [21].

As a reference scenario for our numerical simulations, we have chosen the equilibrium profiles from JET discharge #102371, where $n = 0$ modes driven unstable by energetic ions were indeed observed. Our simulations indicate the presence of two distinct Alfvén modes as possible candidates for the interpretation of JET observations: a lower-frequency

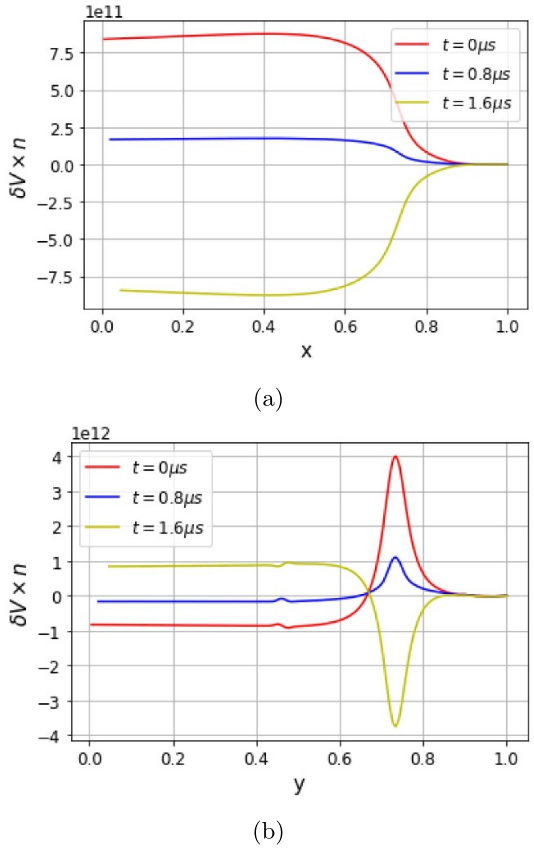


Figure 22. Horizontal component of the perturbed momentum, plotted in (*a*) along a horizontal slice, and in (*b*) along a vertical slice, for different times during one oscillation.

$n = 0$ mode, with a frequency of about 180 kHz, that we have identified as a VDOM, and a higher-frequency $n = 0$ mode, with a frequency of about 310 kHz, that we have identified as a GAE.

An expedient way to investigate damped modes in a numerical simulation of a tokamak plasma, used here for the first time in NIMROD simulations, has been to introduce forced oscillations of the perturbed plasma temperature with a prescribed value of the forcing frequency. When the oscillator frequency matches that of a plasma normal mode, a resonance occurs, which allows the normal mode to grow to a finite amplitude and to be fully resolved numerically. In this way, we can study the normal mode, without relying on carefully selected initial conditions, which facilitates the identification of its distinctive physical properties.

The $n = 0$ mode observed in JET discharge #102371 was excited with a frequency 320 kHz. Thus, if the numerically resolved mode frequency is taken as the only indicator for comparison with experimental data, we are led to conclude that the mode observed in JET shot #102371 is a GAE. However, both GAE and VDOM could be excited in future tokamak experiments, depending on specific plasma conditions. As we have already remarked in the Introduction, our goal in this article is to present, for the first time, the characteristic signatures of VDOM as they appear in a numerical simulation of a realistic tokamak configuration, rather than to provide detailed modelling of particular JET discharges, which will be the subject of a future publication.

Two distinct Alfvén modes were also observed in previous numerical simulations of JET discharges using the MISHKA code [18]; the frequencies of the two modes differed by a factor of about 1.5. The higher-frequency mode was interpreted as a GAE, and the even parity flow found by MISHKA is consistent with the NIMROD simulations presented in this article. The lower-frequency mode was interpreted as an odd-parity GAE. We note that the MISHKA simulations described in [18] lack the open field line region and conducting wall. If, in our NIMROD simulations, we move the perfectly conducting wall to coincide with the plasma last-closed flux surface, the VDOM changes somewhat its characteristics, acquiring a space structure that resembles more closely that of the odd-parity Alfvén mode found by MISHKA. Therefore, we suspect that the odd-parity GAE found by MISHKA and the VDOM found by NIMROD are the same mode. The possible unification of these two interpretations will be considered in a future paper.

Acknowledgments

This work has been carried out within the framework of the EUROfusion Consortium and has received funding from the Euratom Research and Training Programme (Grant Agreement No. 101052200 - EUROfusion). Views and opinions expressed are, however, those of the authors only and do not necessarily reflect those of the European Union or the European Commission. Neither the European Union nor the European Commission can be held responsible for them. This work was partially carried out using EUROfusion High Performance Computer Marconi-Fusion through EUROfusion funding. This research is partially supported by Grant No. 2022BVR09 from the University of Science and Technology of China Visiting Professor International.

We would also like to gratefully acknowledge Eni S.p.A. for the use of their High Performance Computing facility, where NIMROD simulations were carried out, and Claudio Carati of Eni S.p.A. for his interest in our work.

T. Barberis and F. Porcelli would like to acknowledge with thanks the hospitality they received at JET, at GA, and at USTC, where part of their work was carried out.

ORCID iDs

T. Barberis https://orcid.org/0000-0002-1030-7642
F. Porcelli https://orcid.org/0000-0002-3625-6417
D. Banerjee https://orcid.org/0000-0002-7882-6369
Y.Q. Liu https://orcid.org/0000-0002-8192-8411
H.J.C. Oliver https://orcid.org/0000-0002-7302-085X
S.E. Sharapov https://orcid.org/0000-0001-7006-4876
A. Yolbarsop https://orcid.org/0000-0001-7686-0742

References

[1] Hutchinson I. 1989 *Nucl. Fusion* **29** 2107
[2] Lister J. *et al* 1990 *Nucl. Fusion* **30** 2349
[3] Laval G., Pellat R. and Soule J.L. 1974 *Phys. Fluids* **17** 835
[4] Wesson J. 1978 *Nucl. Fusion* **18** 87–132
[5] Barberis T., Yolbarsop A. and Porcelli F. 2022 *J. Plasma Phys.* **88** 905880511
[6] Lazarus E.A., Lister J.B. and Neilson G.H. 1990 *Nucl. Fusion* **30** 111
[7] Albanese R., Mattei M. and Villone F. 2004 *Nucl. Fusion* **44** 999
[8] Villone F., Riccardo V. and Sartori F. (JET-EFDA Contributors) 2005 *Nucl. Fusion* **45** 1328
[9] Portone A. 2017 *Nucl. Fusion* **57** 126060
[10] Okabayashi M. and Sheffield G. 1974 *Nucl. Fusion* **14** 263–5
[11] Rebhan E. 1975 *Nucl. Fusion* **15** 277
[12] Haas F.A. 1975 *Nucl. Fusion* **15** 407
[13] Perrone M. and Wesson J. 1981 *Nucl. Fusion* **21** 871
[14] Fitzpatrick R. 2009 *Phys. Plasmas* **16** 012506
[15] Zakharov L.E., Galkin S.A. and Gerasimov S.N. (JET-EFDA Contributors) 2012 *Phys. Plasmas* **19** 055703
[16] Clauser C.F., Jardin S.C. and Ferraro N.M. 2019 *Nucl. Fusion* **59** 126037
[17] Porcelli F., Barberis T. and Yolbarsop A. 2023 *Fundamen. Plasma Phys.* **5** 100017
[18] Oliver H.J.C., Sharapov S.E., Breizman B.N. and Zheng L.J. 2017 *Phys. Plasmas* **24** 122505
[19] Kiptily V. *et al* (JET Contributors) 2021 *Nucl. Fusion* **61** 114006
[20] Villard L. and Vaclavik J. 1997 *Nucl. Fusion* **37** 351
[21] Barberis T., Porcelli F. and Yolbarsop A. 2022 *Nucl. Fusion* **62** 064002
[22] Banerjee D., Kim C.C., Barberis T. and Porcelli F. 2024 *Phys. Plasmas* **31** 023904
[23] Sovinec C., Glasser A., Gianakon T., Barnes D., Nebel R., Kruger S., Plimpton S., Tarditi A. and Chu M. (the NIMROD Team) 2004 *J. Comput. Phys.* **195** 355
[24] Barberis T. and Porcelli F. 2024 *Plasma Phys. Control. Fusion* **66** 075007
[25] Van Zeeland M.A. *et al* 2021 *Nucl. Fusion* **61** 066028
[26] Strauss H.R. 1976 *Phys. Fluids* **19** 134
[27] Yolbarsop A., Porcelli F. and Fitzpatrick R. 2021 *Nucl. Fusion* **61** 114003
[28] Yolbarsop A., Porcelli F., Liu W. and Fitzpatrick R. 2022 *Plasma Phys. Control. Fusion* **64** 105002
[29] Lao L., John H.S., Stambaugh R., Kellman A. and Pfeiffer W. 1985 *Nucl. Fusion* **25** 1611
[30] O'Brien D., Lao L., Solano E., Garribba M., Taylor T., Cordey J. and Ellis J. 1992 *Nucl. Fusion* **32** 1351
[31] Cooley J.W. and Tukey J.W. 1965 *Math. Comput.* **19** 297–301